

Advances in surface-wave tomography for near-surface applications

*Original*

Advances in surface-wave tomography for near-surface applications / Papadopoulou, M.; Khosro Anjom, F.; Karimpour, M.; Socco, V. L.. - In: THE LEADING EDGE. - ISSN 1070-485X. - ELETTRONICO. - 40:8(2021), pp. 567-575. [10.1190/tle40080567.1]

*Availability:*

This version is available at: 11583/2926858 since: 2021-09-23T18:14:00Z

*Publisher:*

Society of Exploration Geophysicists

*Published*

DOI:10.1190/tle40080567.1

*Terms of use:*

This article is made available under terms and conditions as specified in the corresponding bibliographic description in the repository

*Publisher copyright*

SEG postprint/Author's Accepted Manuscript e/o postprint versione editoriale/Version of Record

Copyright ©SEG. This article may be downloaded for personal use only in accordance with SEG terms of use and conditions. This article appeared in THE LEADING EDGE, 2021, 40, 8, and may be found at SEG Library at <http://dx.doi.org/10.1190/tle40080567.1>.

(Article begins on next page)

# Advances in surface-wave tomography for near-surface applications

Myrto Papadopoulou<sup>1</sup>, Farbod Khosro Anjom<sup>1</sup>, Mohammad Karim Karimpour<sup>1</sup>, and Valentina Laura Socco<sup>1</sup>

<https://doi.org/10.1190/tle40080567.1>

## Abstract

Surface-wave (SW) tomography is a technique that has been widely used in the field of seismology. It can provide higher resolution relative to the classical multichannel SW processing and inversion schemes that are usually adopted for near-surface applications. Nevertheless, the method is rarely used in this context, mainly due to the long processing times needed to pick the dispersion curves as well as the inability of the two-station processing to discriminate between higher SW modes. To make it efficient and to retrieve pseudo-2D/3D S-wave velocity ( $V_S$ ) and P-wave velocity ( $V_P$ ) models in a fast and convenient way, we develop a fully data-driven two-station dispersion curve estimation, which achieves dense spatial coverage without the involvement of an operator. To handle higher SW modes, we apply a dedicated time-windowing algorithm to isolate and pick the different modes. A multimodal tomographic inversion is applied to estimate a  $V_S$  model. The  $V_S$  model is then converted to a  $V_P$  model with the Poisson's ratio estimated through the wavelength-depth method. We apply the method to a 2D seismic exploration data set acquired at a mining site, where strong lateral heterogeneity is expected, and to a 3D pilot data set, recorded with state-of-the-art acquisition technology. We compare the results with the ones retrieved from classical multichannel analysis.

## Introduction

Surface-wave (SW) methods are becoming more popular in a wide range of applications. In near-surface studies, SW investigation is normally based on multichannel processing in which the seismic traces recorded by an array of receivers are used to retrieve a single dispersion curve (DC), which is inverted to estimate a 1D  $V_S$  model (Foti et al., 2015). To map possible lateral variability, several DCs are usually extracted from narrow spatial receiver windows and are inverted to estimate a set of spatially distributed 1D  $V_S$  models (e.g., Bergamo et al., 2012). This approach, although fast and straightforward, may suffer from low lateral resolution because the retrieved velocity models are representative only of the average properties below the receiver spatial window, while possible local velocity variations are smoothed.

On the other hand, SW tomography, a technique widely used in the field of global seismology to image the earth's structure (e.g., Ritzwoller and Levshin, 1998; Kennett and Yoshizawa, 2002; Shapiro and Campillo, 2004; Sabra et al., 2005), can provide higher lateral resolution. The method uses DCs extracted between different pairs of receivers and treats them as average slowness along the receiver path. The curves are inverted simultaneously by discretizing the area into grid points and estimating

either the local phase velocity (e.g., Yao et al., 2006) or the S-wave velocity ( $V_S$ ) (e.g., Boschi and Ekström, 2002; Boiero, 2009) at each location.

With the number of receivers typically used in near-surface studies, a great number of DCs (assuming  $N$  receivers) widely distributed in space with a high degree of path overlap can be extracted. Such high coverage permits the estimation of a shallow pseudo-2D or 3D (depending on the acquisition geometry) velocity model with great detail (e.g., Swoboda et al., 2013; Socco et al., 2014). However, to make it convenient for near-surface applications, automation of the processing (DC estimation) stage is necessary. At the same time, processing should overcome the inherent spatial aliasing issues (e.g., Rosenblad and Li, 2009; Foti et al., 2011) and the high instability (Park and Ryden, 2007) of the two-station technique.

In addition, processing should account for the presence of higher SW modes in the data, which can be expected in a variety of near-surface environments (Foti et al., 2018) and can provide information on deeper layers because they usually present longer wavelengths (Ganji et al., 1998). Although multichannel processing usually provides adequate spectral resolution for the separation of different modes, this is not possible with the two-station method (Halliday and Curtis, 2008) unless a preprocessing technique to isolate the different modes (Dziewonski and Hales, 1972) is applied prior to DC extraction.

Finally, to achieve a comprehensive characterization of the near surface, the estimation of P-wave velocity ( $V_P$ ) is required in addition to the  $V_S$  model estimated with SW tomography. A possible approach to retrieve  $V_P$  is the method of Socco and Comina (2017) and Khosro Anjom et al. (2019), which estimates Poisson's ratio ( $\nu$ ) with multichannel SW processing. The method finds the relationship between the SW propagation wavelength and investigation depth (wavelength-depth relationship [W/D]), which is sensitive to the value of  $\nu$  and can be used for its estimation.

In this work, we demonstrate that SW tomography can be a powerful tool for near-surface characterization by using two case studies. The first example is a 2D seismic mineral exploration data set from a site where strong lateral variations exist in the shallow layers. The second example is a 3D pilot data set recorded with state-of-the-art acquisition technology. We apply a preprocessing scheme to separate multiple SW modes. The path-average DCs of each mode are estimated with a fully data-driven technique, which is completely automatic and does not require the intervention of the operator at any processing step. The curves are inverted with SW tomography for  $V_S$ , and W/D is applied to estimate  $\nu$  and convert  $V_S$  to  $V_P$ .

<sup>1</sup>Politecnico di Torino, Torino, Italy. E-mail: myrto.papadopoulou@polito.it; khosro-anjom.farbod@polito.it; mohammadkarim.karimpour@polito.it; valentina.socco@polito.it.

## Method

The method is presented in Figure 1. To avoid higher-mode contamination in the two-station processing, a set of multichannel DCs is preliminarily estimated from the data and defines the velocity limit between each mode. Based on this limit, the traces are muted to isolate each mode before the two-station processing. The DCs of each mode are then separately estimated between receiver pairs with an automatic data-driven technique, and they are inverted in a tomographic framework. A set of  $v$  profiles is estimated through the W/D method and is used to convert the tomographic  $V_s$  model to  $V_p$ . In the following, the main stages of the workflow are described sequentially.

**Multichannel DC extraction and reference  $V_s$  and  $v$  estimation with W/D.** A set of multichannel DCs is extracted from subsets of receivers selected using a moving spatial window. The dispersion image is computed using the phase shift method (Park et al., 1998), and the DCs' fundamental and higher modes (if excited) are picked as the maxima on each dispersion image (Figure 1a). Using the multimode DCs as a guide, the user defines the velocity limit between the different modes. Among the multichannel DCs, the highest-quality fundamental mode (onward reference curve) is selected according to the quality index defined by Karimpour (2018) and used in the W/D process (Figure 1b). The reference DC is inverted to estimate a 1D  $V_s$  model, and following Socco et al. (2017), the reference curve and  $V_s$  are combined to provide the W/D relationship. Next, following Socco and Comina (2017) and Khosro Anjom et al. (2019), the W/D relationship is used to estimate a 1D  $v$  profile that is considered to be representative of the entire investigated area. In the case of strong lateral variations, the multichannel DCs can be clustered to estimate more than one reference model.

**Automatic multimodal two-station SW processing and tomographic  $V_s$  model estimation.** For each pair of receivers in line with a source, we apply a fully data-driven automatic version of the two-station technique of Bloch and Hales (1968). In the simple case of single-mode excitation, the traces undergo narrow band-pass filtering at different central frequencies following Dziewonski and Hales (1972). A cross-correlation matrix is built by computing the cross correlation of the filtered traces at each frequency. The DC is picked on the matrix with the automatic technique of Papadopoulou (2021), which performs a search for the amplitude maxima closest to the multichannel DC (output in step A). The maxima are picked within a predefined frequency band, and possible erroneous data points are rejected through a series of data-driven quality-control tests. In particular, an automatic screening detects and rejects unreliable frequency bands, searching for abrupt changes in the phase velocity and cross-correlation amplitude (a detailed description can be found in Papadopoulou [2021]).

If higher modes have been detected during the multichannel analysis (step A), we initially isolate the signal corresponding to the desired mode by muting the traces in time domain (Figure 1c) based on the velocity limit estimated in step A. The muted traces containing the signal of a specific mode are input to two-station processing. This process is performed separately for each mode and leads to a set of multimode two-station DCs.

The two-station DCs are input into the SW tomography. We use the technique of Boiero (2009), which is a fast and efficient iterative damped least-squares inversion algorithm, suitable for both pseudo-2D and 3D  $V_s$  model estimation. The inversion requires an initial model, defined as a set of 1D profiles, distributed on a

regular grid across the investigated area. The grid dimensions are set based on the data coverage, desired resolution, and available computational resources (see Garofalo, 2014). To define the initial model  $V_s$ ,  $v$ , and thickness ( $h$ ), we use the reference models estimated in step B. If lateral heterogeneity has been detected, the reference models estimated for each multichannel DC cluster are considered at the corresponding grid points. Available a priori information (e.g., lithological information, borehole/logging data, and other geophysical measurements) can be used as a guide to define the layer density ( $\rho$ ).

For the inversion, each data point is weighted based on its wavelength, and the weights are associated to the covariance matrix. This provides a solution to the fact that for a uniform DC frequency sampling, short wavelengths present a denser distribution and can drive the inversion update only to the shallowest portions of the model (Khosro Anjom et al., 2021). For the inversion regularization, constraints

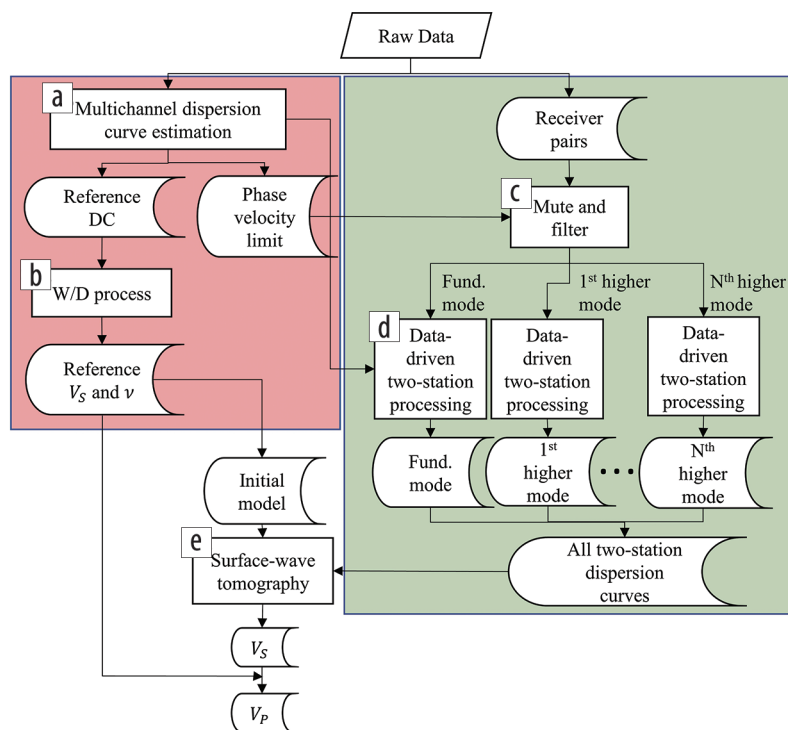


Figure 1. The workflow of the proposed multimodal SW tomography.



for the maximum allowable property variation among two neighboring models and/or layers can be set. In the absence of a priori information on the property variability of the site, the constraints can be defined as the strongest constraints that do not increase the final model misfit (Boiero, 2009). Once the  $V_s$  model has been estimated, it is converted to  $V_p$  based on the reference  $v$ .

### Application to field data

**Ludvika mining site, Sweden.** We present the application of the proposed method to a portion of a large-scale 3D seismic mineral exploration data set acquired in 2019 in the iron-oxide mining site of Ludvika in central Sweden (Figure 2a). The data acquisition (see Malehmir et al., 2021) was performed to estimate the depth extension of the mineralization, known to be formed mainly as sheet-like horizons of magnetite and hematite within dacitic to andesitic feldspar porphyritic metavolcanic host rocks (Maries et al., 2017).

We applied the presented workflow to a portion of the data set, recorded by 337 receivers (10 Hz cabled vertical geophones spaced 10 m with a total length of 3505 m) along the profile shown in red in Figure 2b. The 218 shots (green in Figure 2b) were generated with a 32 tonne vibrator (20 s sweep length, 10–160 Hz linear sweeps, and three sweeps stacked at each location). The data were recorded in 5 s windows (reduced to 2 s for processing) at a sampling rate of 1 ms (resampled at 2 ms for processing).

In Figure 3a, we show the two-station DC extraction (Figure 1b), using as an example from the data recorded by the two receivers shown in white in Figure 2b. Figure 3a shows the computed cross-correlation matrix. We plot in red the reference multichannel DC, which was used as a guide for the process of step C to pick the cross-correlation maxima (gray in Figure 3a) closest to the reference. Through the data-driven screening, a portion of the data points was rejected, and only the part of the curve shown in blue in Figure 3a was kept for further processing. The same process was repeated for all of the selected receiver pairs, resulting in the 2485 curves shown in Figure 3b.

In Figure 4a, we show the spatial coverage achieved by the DCs, computed as the number of curves crossing each position of the line at each wavelength. It can be observed that high (greater than 90) coverage was achieved in a wide wavelength band (between 25 and 190 m) along the entire line, although a sharp coverage drop exists at distances greater than 1800 m. In this area, the data quality was lower with respect to the rest of the line due to the unavailability of shots (see Figure 2b), and several DCs were rejected by the data-driven screening.

To define the initial model for SW tomography, we assumed 60 model points uniformly distributed along the line, each composed of seven layers

overlying the half-space. The initial model was laterally homogeneous, and its properties were set according to the reference  $V_s$  and  $v$  models estimated by Papadopoulou et al. (2020) (Table 1). In Figure 4b, we show the resulting  $V_s$  model, and in Figure 4c we show its conversion to  $V_p$  using the  $v$  estimated with the W/D method (see Papadopoulou et al., 2020). The P-wave velocities vary between 2800 and 6600 m/s in agreement with the expected values for the lithology of the area according to the downhole information of Maries et al. (2017). Several velocity anomalies can be observed, such as the shallow low-velocity anomaly at

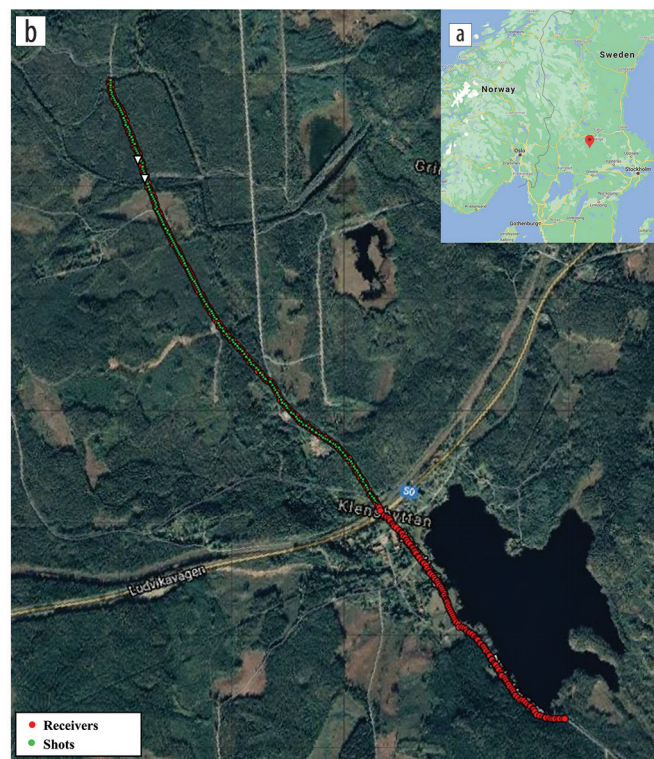


**Figure 2.** (a) Map pointing to the area of interest. (b) Aerial photo of the Blötberget area in central Sweden. The receiver is in red, and the shot geometry is in green. The position of the two receivers used in the example of Figure 3 is in white.

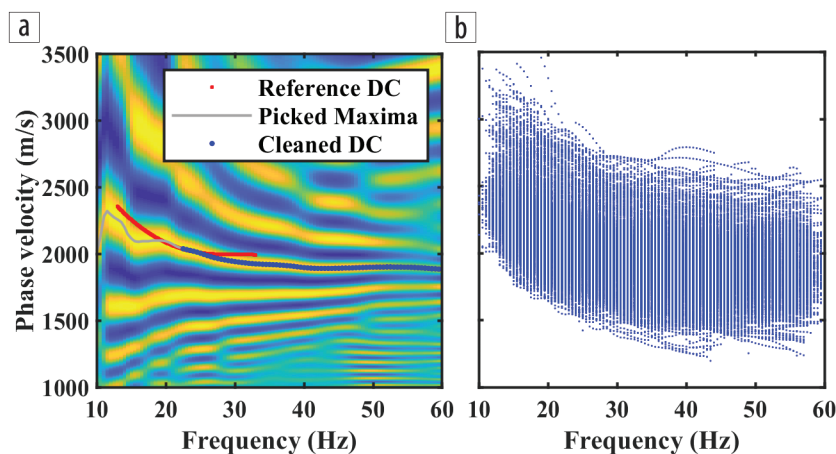


**Figure 3.** (a) Example cross-correlation matrix with the reference curve (red), picked maxima (gray), and cleaned DC (blue). (b) Set of two-station DCs picked for the Ludvika site.

approximately 850 m distance (black arrow in Figures 4b and 4c), corresponding the known location of a water stream that has probably caused fracturing of the rock. The low-velocity anomaly across 1700–2100 m (red arrow in Figures 4b and 4c) and the subsequent rise of the bedrock depth from 2100 to 2600 m distance (green arrow in Figures 4b and 4c) have also been observed by the refraction analysis of Malehmir et al. (2021) and have been interpreted as the result of a normal fault. Finally, the low-velocity anomaly between 2700 and 2900 m distance (magenta arrow in Figures 4b and 4c) probably indicates the shallow expression of a fault, which is assumed to crosscut the mineralization at great depths (Markovic et al., 2020).

### METIS pilot study, Papua New Guinea

We present the results obtained from a 3D seismic data set acquired with a pioneering technology in the framework of the Multiphysics Exploration Technologies Integrated System (METIS) research project (Lys et al., 2018; Pagliccia et al., 2018) in a forest area in Papua New Guinea (PNG). The aim of this project was to develop an acquisition system suitable for remote areas with limited accessibility (e.g., foothills and forests). As a

source, a mud gun was used at 25 locations across the area, and the data were recorded by 38 10 Hz geophones dropped from drones at predefined positions (see Khosro Anjom et al., 2021).

An example shot gather recorded by all of the receivers is shown in Figure 5a. The seismogram shows two dispersive events that are clearly separated at large offset (larger than approximately 350 m). A detailed description of the multichannel processing of the data can be found in Khosro Anjom et al. (2021). In total, seven curves were picked, four of which presented a strong first higher mode besides the fundamental. They are shown in Figure 5b, where blue corresponds to the fundamental mode and red to the higher mode. Inversion (not shown here for brevity) of one of the curves with the method of Maraschini and Foti (2010) revealed that the observed higher mode is the first higher mode.

In Figure 5b, we plot in black the manually defined velocity limit separating the two modes. The reference fundamental mode (dashed blue in Figure 5b) was input to the W/D process (Figure 1b), which allowed the estimation of the reference  $V_S$  and  $v$  profiles (Figure 5 in Khosro Anjom et al., 2021) characterizing the entire area.

To separately pick the different modes with the two-station processing, the portions of the traces containing each mode were isolated (Figure 1c) based on the velocity limit (black in Figure 5b). The muted traces containing only the fundamental mode were used to pick the 198 fundamental-mode curves shown in blue in Figures 6a and 6b. The traces containing only the higher mode were used to pick the 168 higher-mode curves shown in red in Figures 6a and 6b. The corresponding fundamental- and higher-mode paths are shown in the respective color in Figure 6c.

Details of the tomographic inversion of the curves can be found in Khosro Anjom et al. (2021). The estimated  $V_S$  model is shown as velocity slices at different depths in Figure 7, while its conversion to  $V_P$  with  $v$  from the W/D process is shown in Figure 8. The  $V_S$  model presents a clear indication of the velocity variability down to 90 m, while the  $V_P$  model is available down to the depth of the estimated  $v$  (70 m). Because the acquisition was performed at a virgin area where, to our knowledge, no previous investigations have been performed, no a priori information is available for comparison with the estimated models. We can assume that given the intense rain in the region, which is usually more than 6000 mm per year (McAlpine et al., 1983), shallow aquifers can be expected. The high  $V_P$  between 10 and 30 m depths (Figure 8) can be attributed to shallow saturated media, while the  $V_P$  decrease below 30 m (Figure 8) is probably due to clay-rich soil below the aquifer, creating an unsaturated environment.

**Table 1.** Properties of the initial model used for the Ludvika data set.

	$V_S$ (m/s)	$\rho$ (kg/m <sup>3</sup> )	$\nu$ (-)	$h$ (m)
1	3250	2000	0.3	20
2–7	3550	2000	0.3	10
Half-space	4000	2800	0.3	-

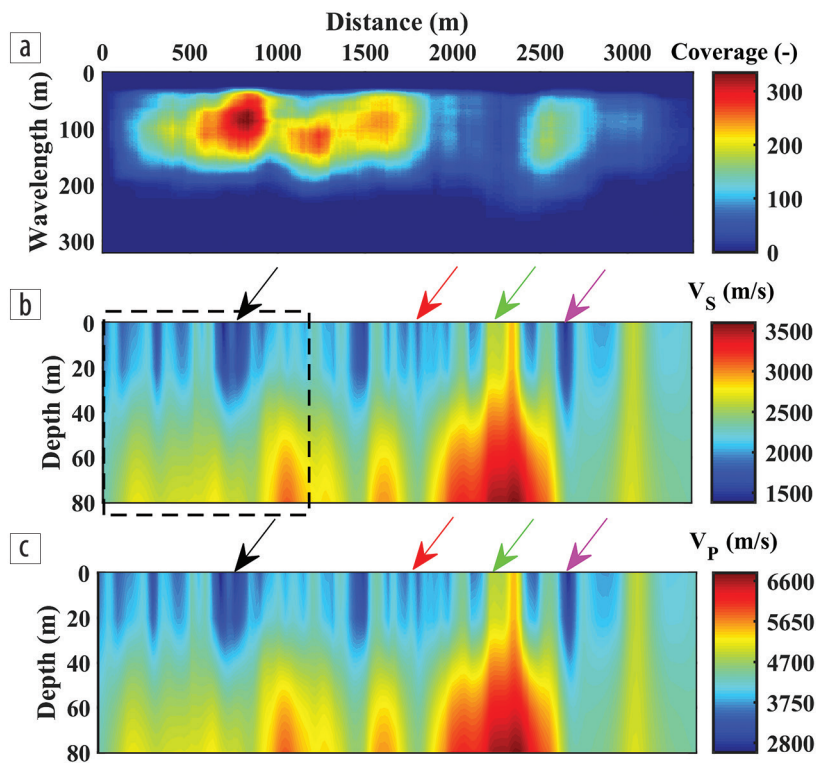


**Figure 4.** (a) DC coverage and estimated (b)  $V_S$  model and (c)  $V_P$  model from the Ludvika site. The box in (b) highlights the position of the models shown in Figures 9b and 9c.



Toward greater depths, the value of  $V_p$  gradually increases until it reaches the maximum velocity (Figure 8) at depths between 60 and 70 m, which we believe coincide with the bed formations. These are comprised mainly of sandstone, siltstone, mudstone, and conglomerates with  $V_p$  of about 2000 m/s (Craig and Warvakai, 2009), which is similar to the estimated velocities. Finally, it can be observed that the model presents lateral variability with higher velocities toward the northeast. The nature of these anomalies will be the matter of future investigation.

## Discussion

Our examples have proven that SW tomography can be efficiently used for estimating near-surface  $V_s$  models. Its combination with the W/D technique provides  $V_p$  directly from the SW contained in the data. In the Ludvika case study, dense DC spatial and wavelength coverage was achieved without the involvement of an operator with the fully data-driven two-station DC estimation and enabled high-resolution  $V_s$  model estimation and detailed mapping of the variability along the line. We compare this result with the results of classical multichannel SW analysis performed by Papadopoulou et al. (2020) for the same site (along the portion of the line indicated by the box in Figure 4b). In total, 80 local DCs were picked using 75 m long spatial data windows and are plotted as a function of wavelength in Figure 9a, each at its corresponding location. The phase velocity is given by the color scale. Due to poor data quality caused by the hard rock complex geologic setting, curves could not be extracted along the entire line, leading to the spatial and wavelength gaps observed in Figure 9a. The laterally constrained inversion (LCI) of the curves, performed according to Socco et al. (2009), resulted in the  $V_s$  model shown in Figure 9b corresponding to the DC locations. Although the LCI was performed with a different initial model with respect to the one used for the tomography and the inversion strategy is different, a comparison of the two models can be indicative of the potential of each method. In general, the LCI model presents similar velocities with the ones of the tomographic model at their common positions (inside the box in Figure 4b and plotted again in Figure 9c). Nevertheless, the lateral velocity variability could not be depicted with the same detail. Moreover, unlike the tomographic model, the LCI model presents strong irregularities in the bedrock velocities in the central portion of the line (650–850 m in Figure 9b), probably due to the nonuniform wavelength coverage of the multichannel DCs at the same locations.

For the PNG case study, due to the low number of receivers (38), only a few DCs (two fundamental-mode and four fundamental- and higher-mode curves)

were estimated with multichannel SW analysis (Figure 5b). This number of curves was not sufficient to estimate a 3D velocity model that depicts the lateral variability over the entire 0.2 km<sup>2</sup> area. On the contrary, the 317 DC paths corresponding to the two-station DCs (Figure 6c) fully covered the entire investigation area and enabled the definition of a dense model grid (152 model points) for the tomography. The inclusion of the higher modes was beneficial because although many (greater than 15%) of the picked DCs contained both fundamental and first higher mode

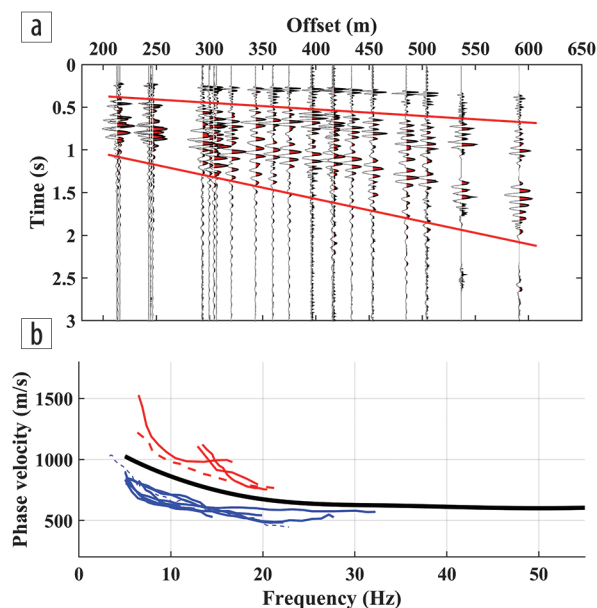


Figure 5. (a) Example shot gather recorded by all of the receivers at the PNG site. (b) Multichannel DCs from the PNG data set. The velocity limit between the fundamental and first higher mode is in black. (Reproduced from Khosro Anjom et al. [2021].)

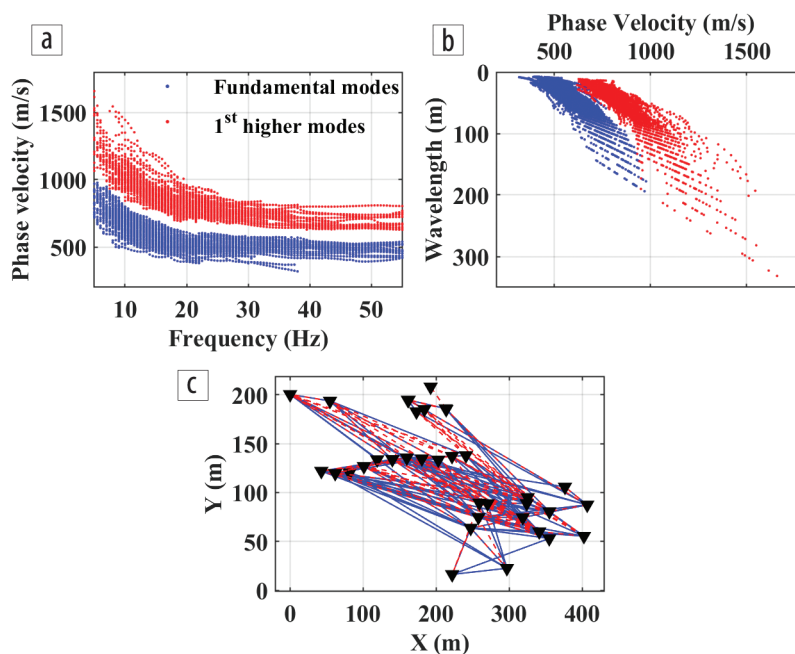


Figure 6. Two-station DCs from the PNG data set, plotted as a function of (a) frequency and phase velocity and (b) wavelength and phase velocity. (c) Path coverage of the picked DCs. (Reproduced from Khosro Anjom et al. [2021].)

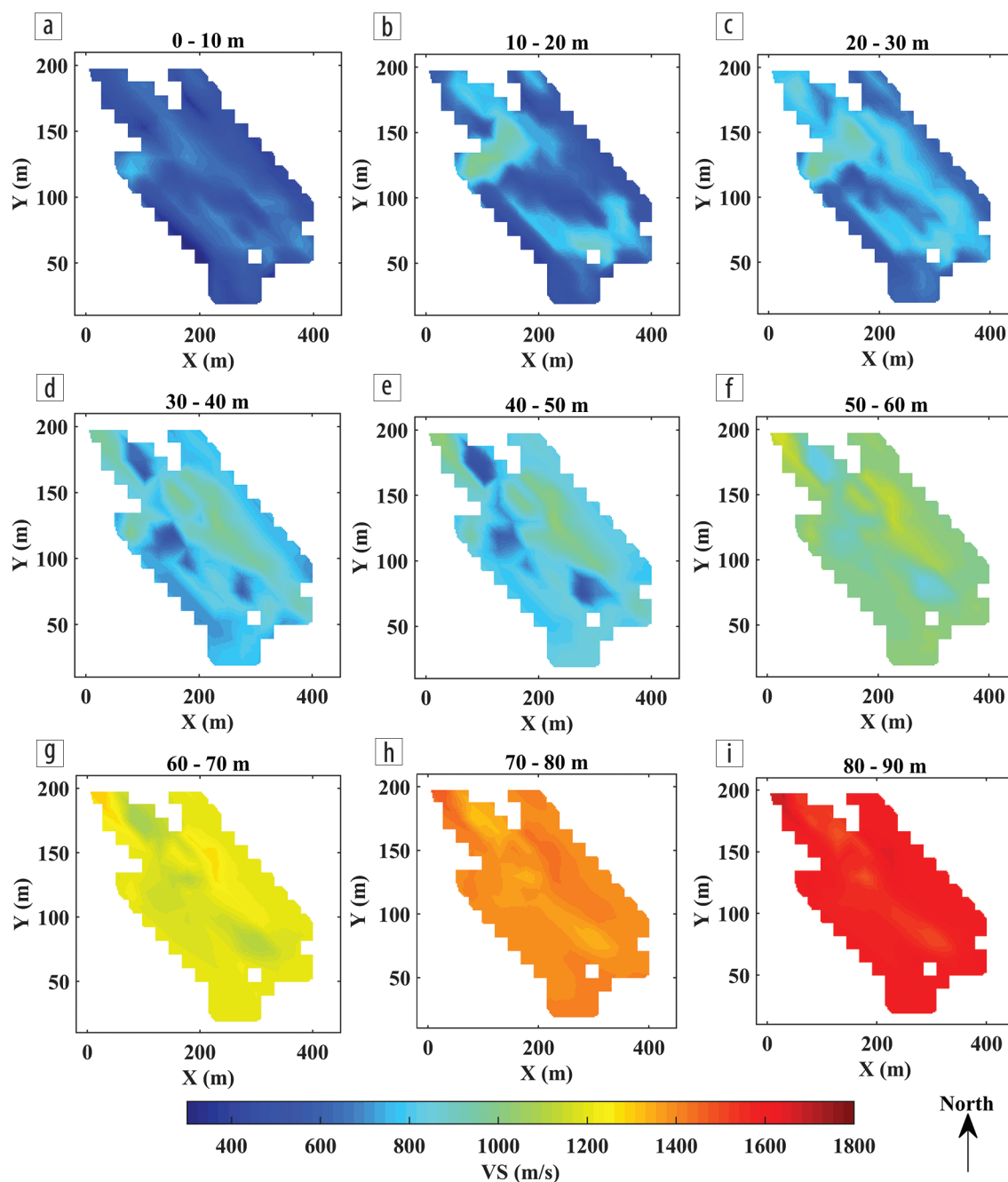


Figure 7. Slices of the estimated  $V_S$  at different depths from the PNG data set (reproduced from Khosro Anjom et al. [2021]).

branches, an amount of 119 paths (red in Figure 6c) were only covered by higher modes, increasing the total path coverage by 60%. Furthermore, Khosro Anjom et al. (2021) have shown that higher-mode inclusion in SW tomography increases the investigation depth due to the longer wavelengths. In the PNG case, the wavelength coverage achieved by both modes was 8–331 m (Khosro Anjom et al., 2021), longer by 137 m with respect to the fundamental-mode wavelengths.

### Conclusion

We have presented an SW tomography workflow that can be efficiently used to estimate high-resolution velocity models for

near-surface applications. The proposed automation of the two-station DC picking allows us to take advantage of the large number of receivers typically used in near-surface applications to maximize the DC coverage at low costs. The tomographic inversion, considering the DCs as path average, benefits from such dense coverage and achieves higher resolution with respect to the classical multichannel approach, which considers local DCs and inverted models. In addition, the proposed approach allows us to retrieve multimode DCs, increasing further the spatial and wavelength DC coverage and improving the quality of the result. Finally, the inclusion of the W/D method in the process allows us to estimate  $V_P$  in addition to  $V_S$  directly from the exploration data in a fast and efficient manner. ■■■

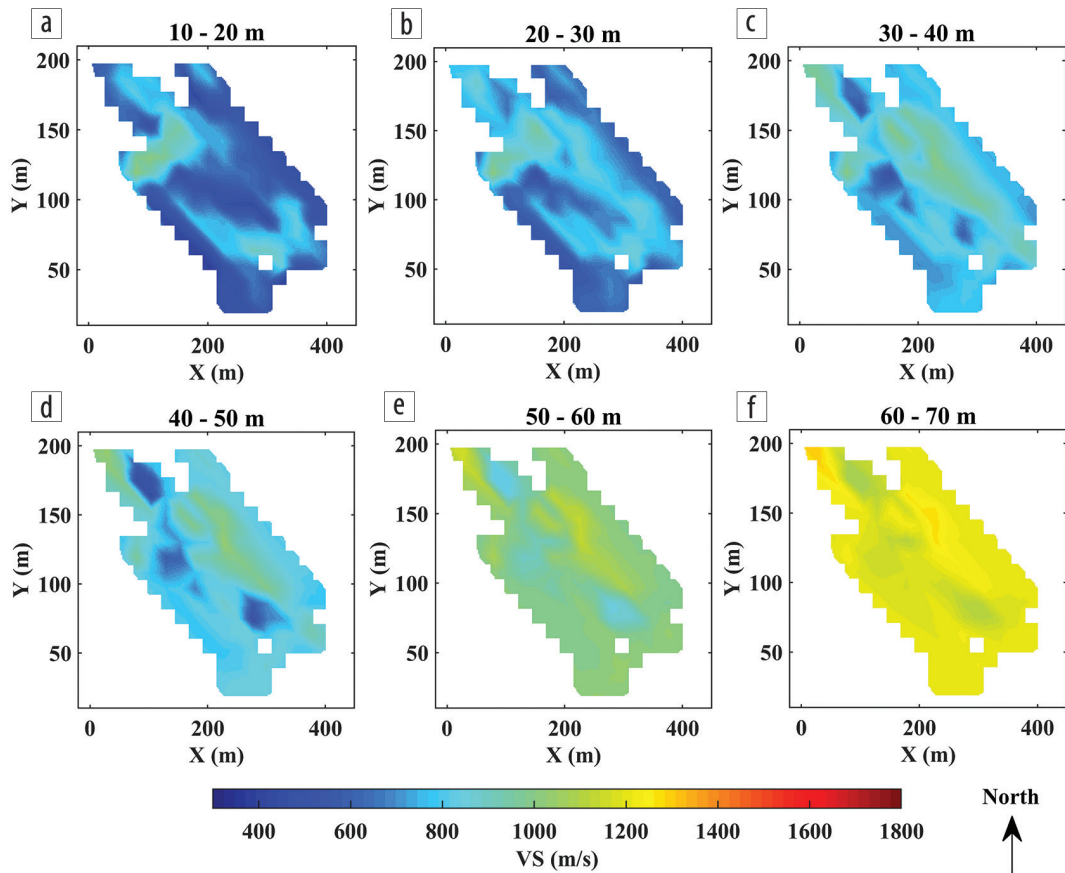


Figure 8. Slices of the estimated  $V_S$  at different depths from the PNG data set (reproduced from Khosro Anjom et al. [2021]).

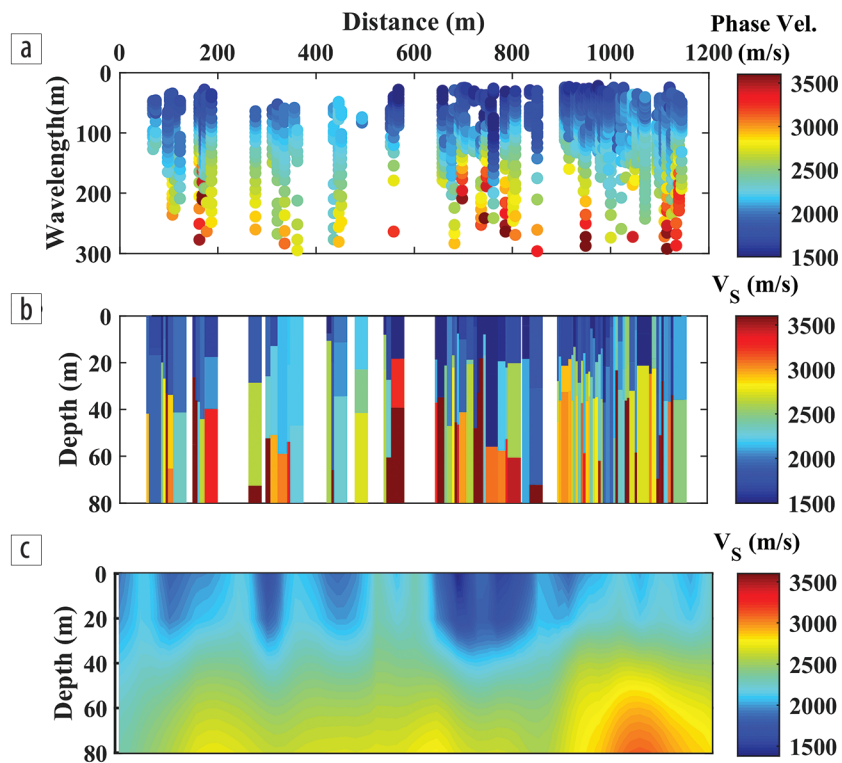


Figure 9. (a) Pseudosection of the multichannel DCs picked for the Ludvika site (reproduced from Papadopoulou et al. [2020]). (b) The  $V_S$  model from the LCI of the curves. (c) The  $V_S$  model from SW tomography at the common location with (b).



## Acknowledgments

We thank Nordic Iron Ore for collaborating with us in this study, conducted through the Smart Exploration project. Smart Exploration has received funding from the European Union's Horizon 2020 research and innovation program under grant agreement no. 775971. The authors would like to thank the METIS team, TOTAL E&P, and SAExploration, as well as TOTAL E&P PNG affiliate, for providing the PNG data set and giving the show right. Farbod Khosro Anjom would like to thank TOTAL E&P for supporting his PhD.

## Data and materials availability

Data associated with this research are confidential and cannot be released.

Corresponding author: myrto.papadopoulou@polito.it

## References

- Bergamo, P., D. Boiero, and L. V. Socco, 2012, Retrieving 2D structures from surface-wave data by means of space-varying spatial windowing: *Geophysics*, **77**, no. 4, EN39–EN51, <https://doi.org/10.1190/geo2012-0031.1>.
- Bloch, S., and A. L. Hales, 1968, New techniques for the determination of surface wave phase velocities: *Bulletin of the Seismological Society of America*, **58**, no. 3, 1021–1034.
- Boiero, D., 2009, Surface wave analysis for building shear wave velocity models: PhD thesis, Politecnico di Torino.
- Boschi, L., and G. Ekström, 2002, New images of the earth's upper mantle from measurements of surface wave phase velocity anomalies: *Journal of Geophysical Research: Solid Earth*, **107**, no. B4, <https://doi.org/10.1029/2000JB000059>.
- Craig, M. S., and K. Warvakai, 2009, Structure of an active foreland fold and thrust belt, Papua New Guinea: *Australian Journal of Earth Sciences*, **56**, no. 5, 719–738, <https://doi.org/10.1080/08120090903005360>.
- Dziewonski, A. M., and A. L. Hales, 1972, Numerical analysis of dispersed seismic waves, in B. A. Bolt, ed., *Methods computational physics: Advances in research and applications*: Elsevier, 39–85.
- Foti, S., S. Parolai, D. Albarello, and M. Picozzi, 2011, Application of surface-wave methods for seismic site characterization: *Surveys in Geophysics*, **32**, 777–825, <https://doi.org/10.1007/s10712-011-9134-2>.
- Foti, S., C. G. Lai, G. J. Rix, and C. Strobbia, 2015, *Surface-wave methods for near-surface site characterization*: CRC Press, Taylor and Francis Group.
- Foti, S., F. Hollender, F. Garofalo, D. Albarello, M. Asten, P.-Y. Bard, C. Comina et al., 2018, Guidelines for the good practice of surface wave analysis: A product of the InterPACIFIC project: *Bulletin of Earthquake Engineering*, **16**, 2367–2420, <https://doi.org/10.1007/s10518-017-0206-7>.
- Ganji, V., N. Gucunski, and S. Nazarian, 1998, Automated inversion procedure for spectral analysis of surface waves: *Journal of Geotechnical and Geoenvironmental Engineering*, **124**, no. 8, [https://doi.org/10.1061/\(ASCE\)1090-0241\(1998\)124:8\(757\)](https://doi.org/10.1061/(ASCE)1090-0241(1998)124:8(757)).
- Garofalo, F., 2014, Physically constrained joint inversion of seismic and electrical data for near-surface application: PhD thesis, Politecnico di Torino.
- Halliday, D., and A. Curtis, 2008, Seismic interferometry, surface waves and source distribution: *Geophysical Journal International*, **175**, no. 3, 1067–1087, <https://doi.org/10.1111/j.1365-246X.2008.03918.x>.
- Karimpour, M., 2018, Processing workflow for estimation of dispersion curves from seismic data and QC: MSc thesis, Politecnico di Torino.
- Kennett, B. L. N., and K. Yoshizawa, 2002, A reappraisal of regional surface wave tomography: *Geophysical Journal International*, **150**, no. 1, 37–44, <https://doi.org/10.1046/j.1365-246X.2002.01682.x>.
- Khosro Anjom, F., D. Teodor, C. Comina, R. Brossier, J. Virieux, and L. V. Socco, 2019, Full-waveform matching of  $V_p$  and  $V_s$  models from surface waves: *Geophysical Journal International*, **218**, no. 3, 1873–1891, <https://doi.org/10.1093/gji/ggz279>.
- Khosro Anjom, F., T. J. Browaeys, and L. V. Socco, 2021, Multimodal surface-wave tomography to obtain S- and P-wave velocities applied to the recordings of unmanned aerial vehicle deployed sensors: *Geophysics*, **86**, no. 4, <https://doi.org/10.1190/geo2020-0703.1>.
- Lys, P.-O., METIS team, K. Elder, and J. Archer, 2018, METIS, a disruptive R&D project to revolutionize land seismic acquisition: *Research and Development Petroleum Conference and Exhibition, Extended Abstracts*, 28–31, <https://doi.org/10.1190/RDP2018-41752683.1>.
- Malehmir, A., M. Markovic, P. Marsden, A. Gil, S. Buske, L. Sito, E. Bäckström, M. Sadeghi, and S. Luth, 2021, Sparse 3D reflection seismic survey for deep-targeting iron oxide deposits and their host rocks, Ludvika Mines, Sweden: *Solid Earth*, **12**, 483–502, <https://doi.org/10.5194/se-12-483-2021>.
- Maraschini, M., and S. Foti, 2010, A Monte Carlo multimodal inversion of surface waves: *Geophysical Journal International*, **182**, no. 3, 1557–1566, <https://doi.org/10.1111/j.1365-246X.2010.04703.x>.
- Maries, G., A. Malehmir, E. Bäckström, M. Schön, and P. Marsden, 2017, Downhole physical property logging for iron-oxide exploration, rock quality, and mining: An example from central Sweden: *Ore Geology Reviews*, **90**, 1–13, <https://doi.org/10.1016/j.oregeorev.2017.10.012>.
- Markovic, M., G. Maries, A. Malehmir, J. von Ketelhodt, E. Bäckström, M. Schön, and P. Marsden, 2020, Deep reflection seismic imaging of iron-oxide deposits in the Ludvika mining area of central Sweden: *Geophysical Prospecting*, **68**, no. 1, 7–23, <https://doi.org/10.1111/1365-2478.12855>.
- McAlpine, J. R., G. Keig, and R. Falls, 1983, *Climate of Papua New Guinea*: Australian National University Press.
- Pagliccia, B., K. Dalton, C. Walker, K. Elder, and R. Jenneskens, 2018, METIS hits the ground in Papua New Guinea: A field-proof innovative method to revolutionize onshore seismic acquisition: 80<sup>th</sup> Conference and Exhibition, EAGE, Extended Abstracts, <https://doi.org/10.3997/2214-4609.201801402>.
- Papadopoulou, M., 2021, Surface-wave methods for mineral exploration: PhD thesis, Politecnico di Torino.
- Papadopoulou, M., F. Da Col, B. Mi, E. Bäckström, P. Marsden, B. Brodic, A. Malehmir, and L. V. Socco, 2020, Surface-wave analysis for static corrections in mineral exploration: A case study from central Sweden: *Geophysical Prospecting*, **68**, no. 1, 214–231, <https://doi.org/10.1111/1365-2478.12895>.
- Park, C. B., and N. Ryden, 2007, Historical overview of the surface wave method: *Symposium on the Application of Geophysics to Engineering and Environmental Problems, Extended Abstracts*, 897–909, <https://doi.org/10.3997/2214-4609-pdb.179.0897-909>.
- Park, C., R. Miller, and J. Xia, 1998, Imaging dispersion curves of surface waves on multi-channel record: 68<sup>th</sup> Annual International Meeting, SEG, Expanded Abstracts, 1377–1380, <https://doi.org/10.1190/1.1820161>.
- Ritzwoller, M. H., and A. L. Levshin, 1998, Eurasian surface wave tomography: Group velocities: *Journal of Geophysical Research*, **103**, no. B3, 4839–4878.
- Rosenblad, B. L., and J. Li, 2009, Performance of active and passive methods for measuring low-frequency surface wave dispersion curves: *Journal of Geotechnical and Geoenvironmental Engineering*, **135**, no. 10, 1419–1428, [https://doi.org/10.1061/\(ASCE\)GT.1943-5606.0000100](https://doi.org/10.1061/(ASCE)GT.1943-5606.0000100).
- Sabra, K. G., P. Gerstoft, P. Roux, W. Kuperman, and M. C. Fehler, 2005, Surface wave tomography from microseisms in Southern

- California: *Geophysical Research Letters*, **32**, no. 14, <https://doi.org/10.1029/2005GL023155>.
- Shapiro, N. M., and M. Campillo, 2004, Emergence of broadband Rayleigh waves from correlations of the ambient seismic noise: *Geophysical Research Letters*, **31**, no. 7, <https://doi.org/10.1029/2004GL019491>.
- Socco, L., D. Boiero, S. Foti, and R. Wisén, 2009, Laterally constrained inversion of ground roll from seismic reflection records: *Geophysics*, **74**, no. 6, G35–G45, <https://doi.org/10.1190/1.3223636>.
- Socco, L. V., D. Boiero, P. Bergamo, F. Garofalo, H. Yao, R. D. van der Hilst, and F. Da Col, 2014, Surface wave tomography to retrieve near surface velocity models: 84<sup>th</sup> Annual International Meeting, SEG, Expanded Abstracts, 2013–2018, <https://doi.org/10.1190/segam2014-1278.1>.
- Socco, L., and C. Comina, 2017, Time-average velocity estimation through surface-wave analysis: Part 2 — P-wave velocity: *Geophysics*, **82**, no. 3, U61–U73, <https://doi.org/10.1190/geo2016-0368.1>.
- Socco, L., C. Comina, and F. Khosro Anjom, 2017, Time-average velocity estimation through surface-wave analysis: Part 1 — S-wave velocity: *Geophysics*, **82**, no. 3, U49–U59, <https://doi.org/10.1190/geo2016-0367.1>.
- Swoboda, U., S. Uchtmann, K. Limbrock, R. Elsen, D. Orłowsky, K. Telenga, A. Koschare, and F. Wollnik, 2013, Seismic and geoelectric investigation of historical mining structures — A case study: 19<sup>th</sup> European Meeting of Environmental and Engineering Geophysics, EAGE, Extended Abstracts, <https://doi.org/10.3997/2214-4609.20131383>.
- Yao, H., R. D. van der Hilst, and M. V. de Hoop, 2006, Surface-wave array tomography in SE Tibet from ambient seismic noise and two-station analysis — I. Phase velocity maps: *Geophysical Journal International*, **166**, no. 2, 732–744, <https://doi.org/10.1111/j.1365-246X.2006.03028.x>.